

Original article

Efforts to untie the multicollinearity knot and identify factors controlling macropore structures in shale oil reservoirs

Ziyi Wang¹, Lin Dong¹✉*, Zhijun Jin^{1,2}, Shuangmei Zou³, Jinhua Fu⁴, Rukai Zhu⁵

¹School of Earth and Space Sciences, Peking University, Beijing 100871, P. R. China

²Institute of Energy, Peking University, Beijing 100871, P. R. China

³School of Earth Resources, China University of Geosciences (Wuhan), Wuhan 430074, P. R. China

⁴PetroChina Changqing Oilfield Company, Xi'an 710018, P. R. China

⁵Research Institute of Petroleum Exploration & Development, PetroChina, Beijing 100083, P. R. China

Keywords:

Shale oil reservoir
macropore
controlling factor
multi-lithology
multi-correlation

Cited as:

Wang, Z., Dong, L., Jin, Z., Zou, S., Fu, J., Zhu, R. Efforts to untie the multicollinearity knot and identify factors controlling macropore structures in shale oil reservoirs. *Advances in Geo-Energy Research*, 2024, 11(3): 194-207.

<https://doi.org/10.46690/ager.2024.03.04>

Abstract:

Traditional correlation analyses based on whole-rock data have limitations in discerning pore development determinants in shale oil reservoir, given the complex lithology of shale formations and intricate interdependencies (multicollinearity) among geological variables. In this study, mercury injection capillary pressure and digital analysis of scanning electron microscopy were employed to examine the macropore structures of both whole rocks and their constituent lithologies for the Upper Triassic Chang-7 shale of the Ordos Basin. Variations were observed among clay shale (shale primarily consisting of clay-sized mineral grains), massive siltstone and silty laminae within the Chang-7 shale. Through the combination of correlation analysis and scanning electron microscope digital technique, it was demonstrated that total organic carbon content primarily controls the level of macropore development, while lithology primarily governs macropore types and structures. Although quartz and pyrite exhibit correlations with macropore volume, they do not emerge as primary factors; instead, they appear interconnected to total organic carbon. Due to detrital mineral framework preservation during compaction, larger macropores are more developed in massive siltstones and silty laminae than in clay shale. Additionally, silty laminae, situated closer to the source rock and influenced by organic acids, exhibit a higher abundance of larger dissolution pores, potentially favoring shale oil development. This study overcomes traditional method constraints, disentangling multi-correlations, and providing new insights into shale macropore development mechanisms, potentially advancing shale oil exploration and production.

1. Introduction

In shale reservoirs, pores can be categorized as micropores (< 2 nm), mesopores (2-50 nm) and macropores (> 50 nm) (Sing et al., 1985), with mesopores (e.g., the Bakken shale in the northern United States (Liu et al., 2018)) or macropores (e.g., the Shahejie shale in the eastern China (Li et al., 2020)) usually accounting for the majority of the porosity. Current shale oil extraction technologies are primarily designed to target the recovery of free oil, which is predominantly stored in macropores (Li et al., 2018; Wu et al., 2021). Thus,

macropores emerge as the dominant reservoirs, and therefore, represent a key target for efficient hydrocarbon recovery. Given these considerations, this study aims to predominantly investigate the characteristics and structures of macropores, along with the key controlling factors influencing their development.

While whole-rock analysis techniques, such as mercury injection capillary pressure (MICP), facilitate a quantitative investigation of overall macropore properties of a shale sample, they lack the specificity required to extract pore-related parameters from discrete segments, such as an ultra-thin silty lamina (only a few hundred micrometers). Shale usually consists of

multiple lithologies (Longman et al., 2016; Su et al., 2018; Fu et al., 2020), and each may exhibit significantly divergent pore characteristics (Gao et al., 2022). Therefore, existing technologies risk overlooking nuanced pore information within specific lithologies. Fortunately, the underutilized technique of digital analysis of scanning electron microscope (SEM) images presents a viable solution to this limitation. This technology can quantitatively extract pore-related parameters, such as surface porosity and pore size distribution, from targeted sampling areas, including distinct lithologies within a whole rock (Liu and Ostadhassan, 2017; Liu et al., 2022).

The intricate relationship between pore characteristics and diverse geological factors presents a complex interplay that demands meticulous investigations. To elucidate the dominant factors governing these pore-related attributes, researchers frequently employ correlation analysis techniques (Tang et al., 2019). Both univariate regression, commonly visualized through scatter plots, and multivariate methods such as partial least squares (PLS) regression emerge as prominent tools for such analyses (Liu et al., 2017; Zhang et al., 2022a). However, it is imperative to acknowledge that the variables related to pores and the geological factors are not completely independent; rather, they frequently demonstrate multicollinearity. This intricate correlation structure can introduce instability and lessen the reliability of coefficient estimates, thereby complicating the accurate interpretation of regression outcomes. While the PLS method excels in addressing mathematical multicollinearity, it falls short in fully discerning the geological interconnections among these factors, let alone uncovering the fundamental geological causation behind them. Essentially, identifying geological factors that exhibit significant correlations with pore-related properties may not necessarily indicate their role as the principal controllers of pore development. Despite the prevalence of studies based solely on correlation analysis to discern controlling influences (Liu et al., 2017; Wang et al., 2021b; Huang et al., 2023), the conclusions drawn from such investigations often give rise to disagreements due to the oversight of multicollinearity. This phenomenon, wherein interdependencies exist among pore-related parameters and geological factors, remains unaddressed. Therefore, a critical validation step necessitates supplementary evidence to fortify the outcomes of correlation analyses. Through the application of SEM quantitative analysis, it becomes feasible to extract data pertaining to surface porosity, the proportion of various pore genetic types, and their size distributions. These data hold the potential to ascertain whether variables displaying noteworthy correlations with pore attributes genuinely exert control over pore development.

The Chang-7 shale formation in the Ordos Basin stands as a pivotal shale reservoir in China, boasting significant resource potential for shale oil extraction (Fu et al., 2020). It is mainly composed of clay shale, massive siltstone and silty laminae (Gao et al., 2022). A series of investigations have been conducted to delve into the characteristics of macropores and their controlling factors of the Chang-7 shale. Prior studies have predominantly performed correlation analysis, revealing a positive correlation between macropore volume and quartz, alongside negative correlations with total organic

carbon (TOC) or pyrite (Han et al., 2018; Huang et al., 2023; Mei et al., 2023). Consequently, a prevailing notion posits that shale macropores are dominantly inorganic, with quartz and pyrite contents playing key roles in the macropore development. However, these studies have overlooked the presence of multicollinearity among geological factors, implying that some identified correlated factors may not actually control the pore development. Moreover, while certain studies have compared pore characteristics across different lithologies, these comparisons are based solely on whole-rock analysis of the samples featuring single lithology or specific lithological combinations (Lu et al., 2021; Wang et al., 2023a, 2023b). This approach falls short in elucidating the intricacies of different pore types, potentially limiting a more profound understanding of pore development mechanisms in distinct lithologies.

This study adopts a comprehensive approach by integrating both MICP and SEM analysis. This combined methodology allows for a quantitative and detailed exploration of the macropore structures present within both whole-rock samples and their distinct lithological constituents in the Chang-7 rock. A pivotal innovation of this study lies in the diligent identification and disentanglement of the intricate web of interrelated geological factors that could otherwise confound analyses. This study has the potential to shed new light on the mechanism of shale macropore development and catalyze advancements in the exploration and production of the Chang-7 shale. Moreover, the methodology utilized in this study may serve as a template for future research endeavors in this domain.

2. Geological setting

Ordos Basin is a Mesozoic intracratonic basin situated in northern China (Fig. 1(a)). It covers a large area of 320,000 km² and is regarded as one of the most important petroliferous basins in China (Guo et al., 2014; Qin et al., 2021). Within this basin, the Upper Triassic Yanchang Formation, characterized by predominantly fluvial, deltaic, and lacustrine deposits, stands out as a focal point for petroleum exploration (Yu et al., 2016; Chen et al., 2019). This formation comprises ten members, referred to as Chang-1 to Chang-10 in descending order (Cao et al., 2016; Fu et al., 2022). Of these members, the Chang-7 member records the most substantial transgression of the Triassic lake system, enlarging the basin's expanse to over 50,000 km² and deepening the water depth to around 150 m. This transgression leads to the deposition of fine grained sedimentary rock, notably organic-rich shale and mudstone (Yang et al., 2010; Fu et al., 2022; Lin et al., 2022). Consequently, the Chang-7 shale emerged as a paramount source rock in the Ordos Basin, characterized by a predominance of type I and II kerogen, with high organic matter content and low-medium maturity (Wang et al., 2022). TOC content mainly ranges from 5% to 23%, and vitrinite reflectance (R_o) values typically span the interval of 0.6% to 1.0% (Cui et al., 2019; Fu et al., 2020; Zhao et al., 2020). In recent years, significant shale oil resource potential has been revealed in the Chang-7 shale (Fu et al., 2022; Hu et al., 2024). The Chang-7 member can be further divided into three units from bottom to top, namely

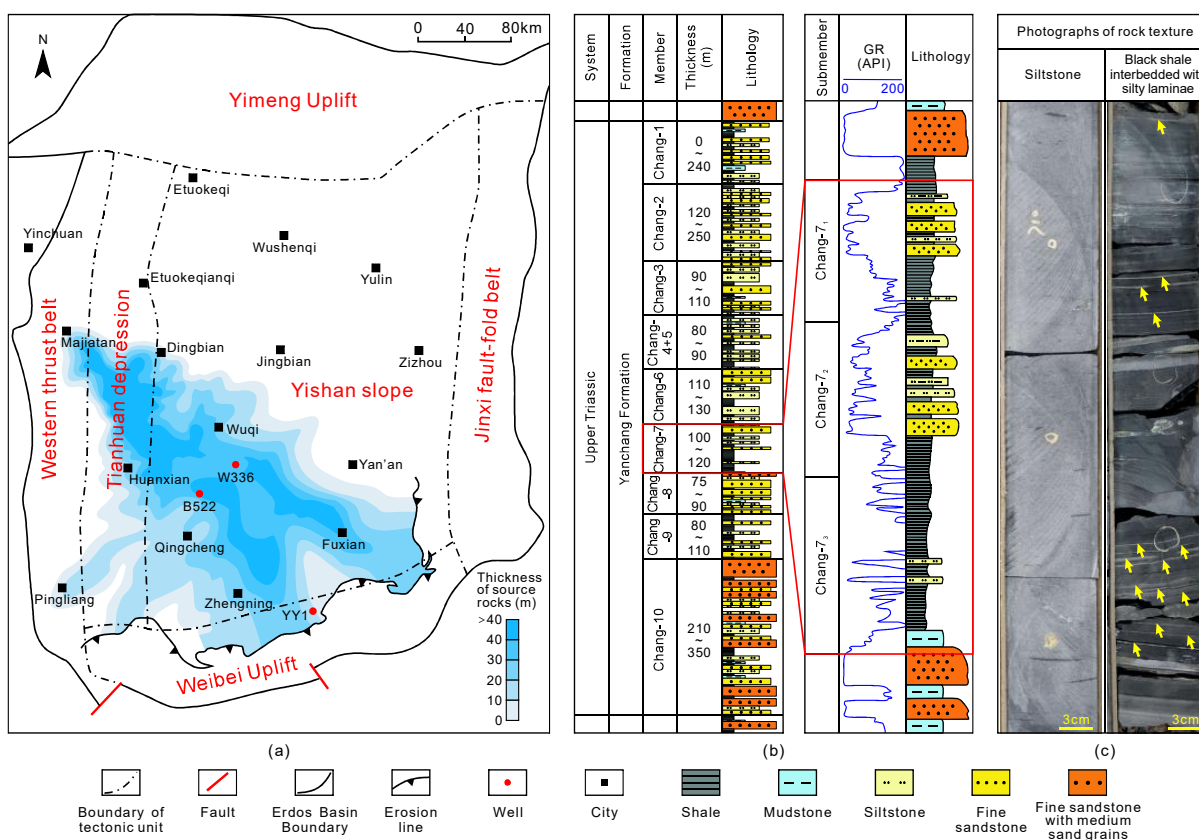


Fig. 1. (a) Geological map of the Ordos Basin illustrating the source rock thickness of the Upper Triassic Chang-7 shale and the locations of the sampling wells, (b) stratigraphic column depicting the Upper Triassic Yanchang formation (modified from Fu et al. (2022)), as well as (c) photographs of rock texture showing siltstone layer (YY1 well, 212.4-213.0 m) and dark-colored shale interbedded with silty laminae indicated by the yellow arrows (YY1 well, 231.6-232.2 m).

Chang-7₃, Chang-7₂ and Chang-7₁ submembers, respectively (Fig. 1(b)). The Chang-7₂ and Chang-7₁ submembers mainly consist of sandstone and siltstone (Fig. 1(c)), interbedded with dark-colored shale. These sandstone and siltstone layers can extend to several meters in thickness and serve as essential reservoirs for shale oil. In contrast, the Chang-7₃ submember predominantly comprises organic-rich black shale, intercalated with silty laminae. These laminae can be quite dense in certain intervals (Fig. 1(c)), typically measuring millimeters in thickness. Unlike the massive sandstone and siltstone in the Chang-7₂ and Chang-7₁ submembers, these silty laminae are situated adjacent to, or within, the source rock (i.e., clay shale). Consequently, the migration distance of the generated shale oil is much shorter. Presently, the commercial efforts directed towards the exploitation of the Chang-7 member predominantly focuses on the Chang-7₁ and Chang-7₂ shales (Cui et al., 2019; Fu et al., 2020).

3. Methods

3.1 Samples

In this study, sixteen core samples of Upper Triassic Chang-7 shale were collected from three wells located in the Ordos Basin (Fig. 1(a)). These samples are composed of

different rock types, including clay shale, massive siltstone and silty laminae (as shown in Figs. 2(a)-2(f) and Table S1). Each core sample was split into two parts, with cuts made perpendicular to layers. One part was crushed to a suitable size for various analyses such as X-ray diffraction (XRD), TOC, R_0 and MICP analyses. The other part was made into thin- and thick-sections for microscopic observation. The surfaces of the thin- and thick-sections represent neighboring cross-sections of the core sample and mirror each other, as shown in Figs. 2(a) and 2(b).

3.2 Mineralogical and organic geochemical analyses

Whole-rock shale powders with size smaller than 100 mesh were analyzed for mineral composition through a Rigaku D/max-2500PC X-ray diffractometer. The X-ray source was a copper target emitting $K\alpha$ radiation (wavelength of 1.5418 Å), operated at 40 kV and 30 mA. Scans were performed at a rate of 2° per minute in terms of the diffraction angle (2θ). Total organic carbon analysis was carried out on the powder samples finer than 100 mesh. The samples were firstly immersed in 5% dilute hydrochloric acid at 60 °C for 24 hours to remove carbonates, and were then rinsed with deionized

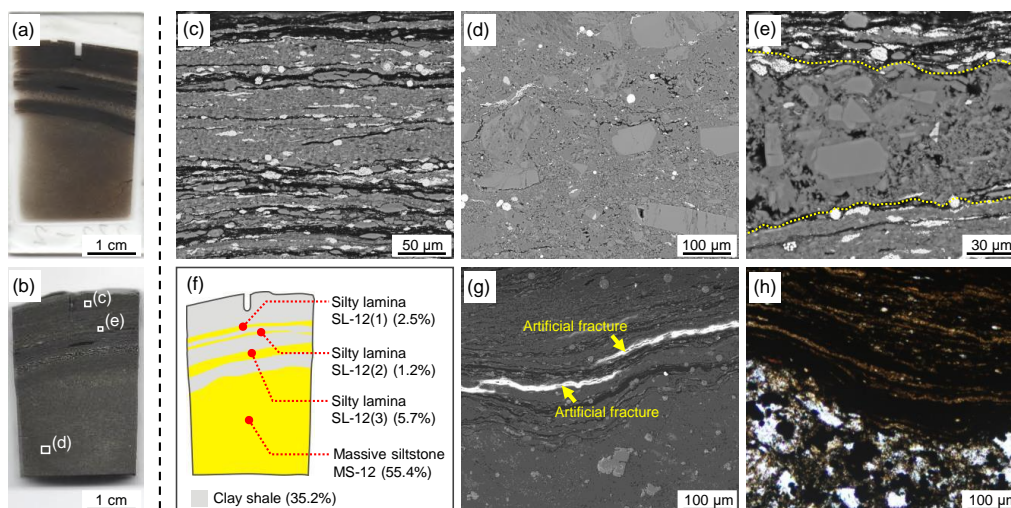


Fig. 2. Thin- and thick-sections pictures as well as photomicrographs of the sample #12, which is composed of three lithologies. The surfaces of the (a) thin- and (b) thick-sections represent two neighboring cross-sections of the core sample, exhibiting a mirror image relationship. (c) Secondary electron photomicrograph of the clay shale. (d) Secondary electron photomicrograph of the massive siltstone. (e) Secondary electron photomicrograph of the silty lamina. The imaging positions are represented by the white rectangles in (b). (f) Schematic diagram showing the area proportions of different lithologies in the profile. (g) Secondary electron photomicrograph showing some fractures can be found in the SEM bulk samples. (h) Transmitted light image of thin section reveals the absence of fractures at corresponding positions to those depicted in (g), showing that the observed fractures in (g) were artificially introduced during the sample pretreatment process.

water until neutral pH was achieved. Next, the carbonate-free samples are dried for 24 hours at 80 °C to a constant weight and were then thoroughly mixed with Fe powder and W-Sn alloy. The mixture powders were then subjected to analysis using a LECO CS230 Elemental Analyzer. Vitrinite reflectance analysis was facilitated through the isolation of kerogen from the whole-rock powders finer than 100 mesh, by employing treatments with HF and HCl. To carry out the measurement, a J&M TIDAS MSP-400 spectrophotometer was employed. For each sample, about 30 individual measurements were executed, ensuring robust statistical representation, with the standard deviations of R_o data remaining within a range of no greater than 0.1%.

3.3 Mercury injection capillary pressure analysis

Whole-rock particle samples with size between 20 and 35 mesh were measured for their macropore volume (i.e., the volume of the all macropore per unit mass whole-rock sample, cm^3/g) based on the mercury injection capillary pressure analysis. Before the measurement, the particle samples firstly underwent a ten-day Soxhlet extraction with a dichloromethane solution to remove the residual oil occluding the pores (Li et al., 2020). Subsequently, the samples were dried at 80 °C for 72 hours until reaching a constant weight. The oil-washed samples were then analyzed using a Micromeritics PoreMaster GT60. When performing MICP testing on particle samples, it is expected that the results will be higher than the true values due to the presence of pores between the sample particles that cause interference. To eliminate this error, a conformance correction was implemented, resulting in more

accurate determinations of macropore volume and macropore size distribution. Detailed methods can be found in Yu et al. (2019).

3.4 PLS regression analysis

PLS-regression analysis was employed to reveal the intricate multivariate correlations between pore attributes and geological factors. This method establishes a linear regression model incorporating orthogonal components derived from standardized independent and dependent variables. This approach serves as a robust tool for conducting multivariate regression analysis in the presence of collinearity (Wold et al., 2001). Furthermore, the method employs the variable importance in projection (VIP) score to gauge each descriptor's incremental contribution to the model component(s), thereby delineating the impact of each on the predicted responses. When a descriptor plays an important role in controlling the component(s), it significantly contributes to elucidating the response and is characterized by a relatively high VIP value. Generally, descriptors with VIP values greater than 1 (the average of square VIP values) are considered pertinent and vital for predicting the response (Favilla et al., 2013; Stocchero et al., 2019). For a comprehensive understanding of the mathematical intricacies, refer to supplementary notes in Supplementary File for detailed information of the calculation methods.

3.5 Microscopic analysis

A comprehensive analysis was undertaken, utilizing a combination of optical and electron microscopy techniques.

Optical microscopy was employed for the scrutiny of thin-sections, and SEM was utilized to examine bulk samples. To prepare bulk samples for SEM, thick-sections were cut into 1.5 cm × 1.5 cm squares. These squares underwent a meticulous process involving oil-washing with a dichloromethane solution over a period of ten days to remove residual oil. Subsequently, the oil-washed samples were subjected to a sequence of polishing stages using diamond powders as fine as 0.5 μm in grain size, followed by the utilization of a PECS II Model 685 argon ion polisher. After these steps, a 5 nm chrome coating was applied to the surfaces of the bulk samples, and they were then examined using a FEI Quanta 650 FEG field-emission scanning electron microscope. The identification of minerals and organic matters via secondary electron and backscatter imaging, coupled with energy spectrum analysis. Pores were discerned through features like relatively high grayscale and the bright edges (Goldstein et al., 2018) in secondary electron images. Based on the digital analysis of SEM images randomly taken from the samples, the surface macroporosity (i.e., the ratio of the macropore area to the SEM quantitative analysis area) and the area ration of organic matter (i.e., the ratio of the organic matter area to the analyzed area) of each lithology were obtained by using Fiji-ImageJ software. By integrating obtained data with lithological proportions, the overall surface macroporosities and area rations of organic matter of the whole-rock samples could be calculated, as indicated in Fig. 2(f).

The process of extracting pores and organic matter was performed based on the grayscale of the SEM images. Initially, these micrographs were manually partitioned into segments, each dedicated to either organic matter or individual pore types. The lassoed portions were subsequently subjected to area extraction using Fiji-ImageJ software, as illustrated in Figs. S1(a)-S1(f). This method enabled us to evaluate the proportion and pore size (measured by minimum Feret diameter) distribution for each pore category, including pores among clay minerals, interparticle pores, intercrystalline pores, dissolution pores, organic pores, and fractures (Fig. S1(g)). It is worth mentioning that some observed fractures in the SEM bulk samples (Fig. 2(g)) were absent in the corresponding positions of the thin sections (Fig. 2(h)). These fractures likely artificial formations during sample pretreatment, and thus, were excluded from quantitative analysis.

For reliability, all SEM images subjected to quantitative analysis possessed resolutions surpassing 0.1032 pixels/nm. The total area of quantitative analysis of the sixteen core samples by SEM exceeded $5.45 \times 10^5 \mu\text{m}^2$. To verify the reliability of this method, correlations were established between whole-rock surface macroporosity and macropore volume gauged through MICP analysis, together with the correspondence between whole-rock area ratio of organic matters and TOC content (see Sections 4.1 and 4.3).

4. Results

4.1 Mineralogy and organic geochemistry

XRD analyses obtained mineral composition within the whole-rock sample from the Chang-7 shale oil reservoirs (Ta-

ble S1). The results indicate that clay minerals are dominant, whose content ranges from 28 to 53 wt% (average of 35.7 wt%). Feldspar, the second-most mineral, is in the content range from 13 to 31 wt% (average of 23.5 wt%). Quartz has a content similar to that of feldspar, in the range from 12 to 34 wt% (average of 23.2 wt%). Followed by pyrite content with average of 11.0 wt%, widely varying from 0 to 35 wt%. Besides, the samples also contain some carbonates (calcite, dolomite and siderite) with the content range from 2 to 20 wt% and average of 6.6 wt%.

Total organic carbon analysis illustrated that the TOC contents of the whole-rock samples are in a wide range from 0.85 to 21.73 wt% (Table S1) and the average TOC content is up to 8.99 wt%. In addition, the organic matter area ratios of the whole rocks and their constituent lithologies were extracted and are presented in Tables S2-S5. Fig. 3(a) depicts a clear positive correlation between the TOC content and the whole-rock area ratio of organic matters quantified by SEM ($R^2 = 0.79$, $P < 0.01$), demonstrating the efficacy of both TOC and SEM analyses in quantifying the degree of organic matter development within the Chang-7 shale. Vitrinite reflectance analysis of isolated kerogen revealed that the samples have R_o values ranging from 0.63% to 0.96%, with an average of 0.73%. The samples collected in this study hold significant representativeness, as their TOC and R_o values encompass nearly the entire range of the TOC content and maturity levels documented in the previous studies pertaining to the Chang-7 shale (Zhao et al., 2018, 2020; Fu et al., 2020).

4.2 Whole-rock macropore volume and its geological correlations

MICP measurements were conducted to determine the macropore volume of the whole-rock samples. The results are presented in Table S2, with values ranging from 0.0027 to 0.0134 cm³/g (average of 0.0071 cm³/g). To reveal the intricate multivariate relationships between macropore volume and geological factors, PLS regression was employed in this study. However, it is important to acknowledge that in the absence of a well-defined physical model elucidating the precise relationship between pore attributes and geological factors, determining the appropriate functional form for PLS-regression analysis is challenging. Previous studies have adopted various approaches to tackle this conundrum. For example, in an examination of the Bakken shale in North America (Liu et al., 2017), linear relationships were assumed across all pore and geological factors, leading to a linear PLS-regression analysis based on the original parameters. In another study focusing on the Shahejie shale in East China (Wang et al., 2021b), researchers contemplated relationships as linear or nonlinear, with the choice of functional forms in the subsequent PLS-regression analysis contingent upon the goodness-of-fit derived from univariate regression models (linear, logarithmic, exponential, and power models). Given the absence of a definitive consensus on the most appropriate functional form, this study embraces the consideration of both assumptions in the two phases of PLS-regression analysis conducted herein. The initial PLS-model, denoted as M1, was

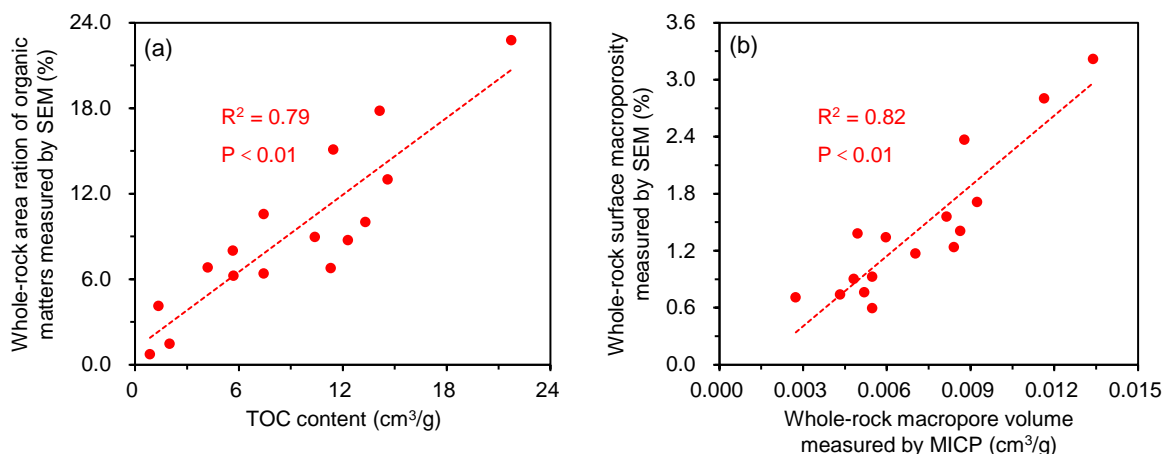


Fig. 3. (a) Evident positive correlation between TOC content and the area ratio of the organic matters measured by SEM for whole-rock samples and (b) evident positive correlation between macropore volume measured by MICP and surface macroporosity measured by SEM for whole-rock samples. Sample size for both figures was sixteen. Statistical significance was established at $p < 0.01$. These indicate that SEM analysis can effectively characterize the variations of the macropores and organic matters in the Chang-7 shale.

obtained by assuming linear correlations between all pore and geological factors. Within this model, the dependent variable is the whole-rock macropore volume, while the independent variables are mineral compositions and TOC contents. The resulting regression equation and VIP values of descriptors are meticulously detailed in Table 1. According to the regression coefficient, quartz, feldspar and carbonates exert a positive influence on macropore volume, whereas clay minerals, pyrite, and TOC exhibit a negative impact. The descriptor TOC emerges as the most influential variable, as indicated by its largest VIP value of 1.38, followed by quartz (1.17), pyrite (1.02), carbonates (0.99), clay minerals (0.78) and feldspar (0.32).

In the second iteration of PLS-regression analysis (PLS-model M2), potential nonlinear relationships among variables were introduced. To facilitate this multivariate analysis, whole-rock macropore volume was cross-plotted against geological factors. As shown in Fig. S2(a), macropore volume exhibits a negative correlation with TOC content. Among the univariate regression models assessed, the logarithmic model yielded the highest coefficient of determination ($R^2 = 0.71$). Consequently, the log-transformed TOC (\ln TOC) was incorporated as an independent variable in the PLS-regression analysis. Figs. S2(b)-S2(f) illustrates the relationships between macropore volume and mineral contents, with macropore volume showing a linear positive correlation with quartz ($R^2 = 0.39$, Fig. S2(b)) and ambiguous correlations with other minerals (Figs. S2(c)-S2(f)). Therefore, original macropore volume and mineral contents were assigned as dependent and independent variables, respectively, in the PLS-regression analysis. Table 1 presents the regression equation and VIP values of the PLS-model M2. Remarkably, the result of this model closely mirrors those of PLS-model M1. Macropore volume continues to exhibit positive correlation with quartz, feldspar, and carbonates, and negative correlation with clay minerals, pyrite, and TOC. The

descriptor of \ln TOC had the largest VIP value (1.59), and the ranking of VIP values for other variables in the model M2 aligns precisely with that of the model M1.

Although the descriptor sets of the PLS-models M1 and M2 are different, both analyses yield remarkably similar results. Compared with model M2 ($R^2 = 0.70$), model M1 boasts a higher coefficient of determination ($R^2 = 0.75$) and thus may be more suitable for analyzing the factors governing macropores in the Chang-7 shale samples. According to the PLS-model M1, several variables, including TOC, quartz, and pyrite exhibit VIP values higher than 1, indicating that these descriptors were relatively more important in characterizing the response.

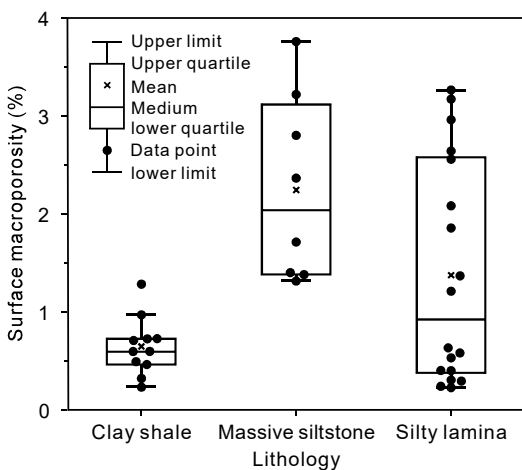
4.3 Microscopic characteristics of macropores in various lithologies

Based on the SEM quantitative analysis, the surface macroporosities of both whole-rock samples and their constituent lithologies were obtained. The values of whole-rock surface macroporosity range from 0.59% to 3.22%, with an average of 1.43% (Table S2). An evident positive correlation between the whole-rock surface macroporosity, as quantified by SEM, and the macropore volume assessed through MICP (Fig. 3(b); $R^2 = 0.82$). This robust correlation underscores the efficacy of both MICP and SEM techniques in quantifying macropore variations in the Chang-7 shale. Consequently, the surface macroporosity data, obtained by SEM quantitative analysis for the diverse lithologies, carries a high degree of reliability.

SEM outcomes reveal distinct ranges of surface macroporosity for different lithological components. Specifically, clay shale exhibits surface macroporosity values ranging from 0.23% to 1.28%, with an average of 0.65% (Fig. 4, Table S3). In contrast, massive siltstone demonstrates a higher spectrum of surface macroporosity, ranging from 1.31% to 3.76%, with

Table 1. Regression coefficients and VIP values of geological factors for the PLS models M1 and M2 of the macropore volumes for the Chang-7 shale in the Ordos Basin.

Descriptors	PLS-model M1		PLS-model M2	
	Regression coefficient	VIP	Regression coefficient	VIP
Constant	8.01×10^{-3}	/	6.87×10^{-3}	/
Clay minerals (wt%)	-1.23×10^{-4}	0.78	-3.17×10^{-4}	0.35
Quartz (wt%)	1.15×10^{-4}	1.17	1.19×10^{-4}	1.18
Feldspar (wt%)	6.87×10^{-5}	0.32	1.92×10^{-4}	0.16
Carbonates (wt%)	1.99×10^{-4}	0.99	1.28×10^{-4}	0.98
Pyrite (wt%)	-4.51×10^{-5}	1.02	-5.93×10^{-4}	0.99
TOC (wt%)	-1.77×10^{-4}	1.38	/	/
ln TOC	/	/	-1.06×10^{-4}	1.59
R ²	0.75		0.70	

**Fig. 4.** Box-plot of the surface macroporosity data of the clay shale, massive siltstone and silty lamina within the Chang-7 shale. The surface macroporosity is quantified by digitally analyzing scanning electron microscope images and calculating the ratio of the total pore area to the entire area investigated.

an average of 2.24% (Fig. 4, Table S4). Silty laminae, on the other hand, broadly cover the ranges observed in both clay shale and massive siltstone, with values ranging from 0.23% to 3.26% and an average of 1.37% (Fig. 4, Table S5).

Leveraging both SEM and energy spectrum analyses, multiple types of pores within the samples were identified. Among these, the most prevalent pore categories encompass pores situated among clay minerals (Fig. 5(a)), interparticle pores (Fig. 5(b)), fractures (Fig. 5(c)), dissolution pores occurring in feldspar (Fig. 5(d)) and carbonates (Fig. 5(e)). In addition to these primary pore types, secondary categories were also observed, including intercrystalline pores found among carbonates (Fig. 5(e)) and pyrites (Fig. 5(f)), pores between mica sheets (Fig. 5(g)), dissolution pores in quartz (Fig. 5(h)) and organic pores (Fig. 5(i)). Furthermore, a quantitative

assessment of the surface macroporosity values associated with each of these pore types was conducted. The quantification process was achieved through digital analysis of SEM images for both whole-rock samples (Table S2) and their constituent lithologies (Tables S3-S5). The proportional distribution of these various pore types is graphically depicted in Fig. 6, offering a comprehensive insight into their respective prevalence within rocks.

For the whole-rock samples (Fig. 6(a)), pores among clay minerals are the most dominant contributor to the macropores, constituting 71.2% of the total surface macroporosity. They are followed by interparticle pore (12.1%), dissolution pores in feldspar (9.5%), fracture (4.3%) and dissolution pores in carbonates (1.8%). Other pore types contribute only a limited proportion of macropores, accounting for just 1.2%. Notably, despite meticulous efforts to identify and exclude artificial fractures generated during sample pretreatment from the quantitative statistics (see Methods section), there may still be some fractures formed during the coring, core transportation and preservation processes, making it challenging to distinguish them from the original fractures within the strata. Therefore, caution is warranted when interpreting the pore data related to fractures. The proportion of fractures in the samples was, however, limited (4.3%), and thus, any errors associated with them have a minimal impact on the total surface macroporosity. Figs. 6(b)-6(d) and 7 illustrate significant variations in both composition and size distribution among distinct types of macropores in clay shale, massive siltstone and silty lamina. These distinctions are crucial for interpreting the origins of pore structures and a comprehensive analysis will be presented in Section 5.3.

5. Discussion

5.1 Multicollinearity and limitation of correlation analysis

The results derived from PLS-model M1 indicate a distinct positive correlation between the macropore volume of whole-

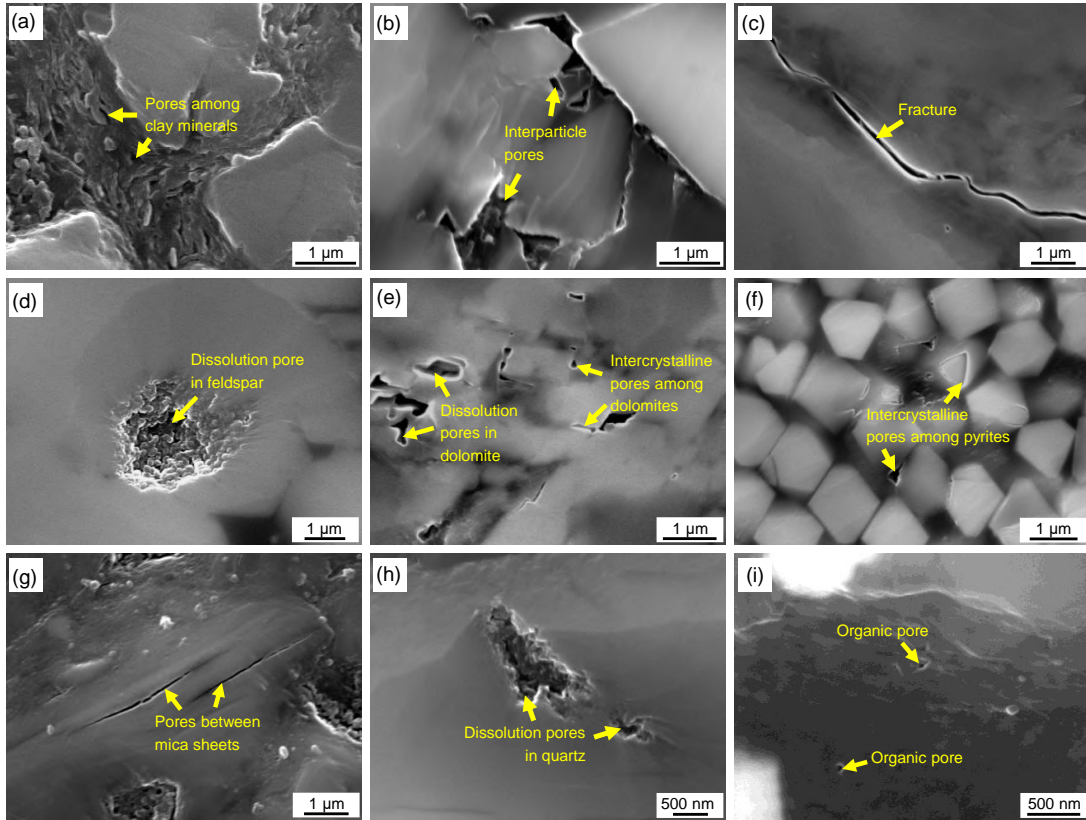


Fig. 5. Secondary electron photomicrographs showing the pore types observed in the Chang-7 shale. (a) Pores among clay minerals, (b) interparticle pores, (c) fractures, (d) dissolution pores in feldspar, (e) dissolution and intercrystalline pores among carbonates, (f) intercrystalline pores among pyrites, (g) pores between mica sheets, (h) dissolution pores in quartz and (i) organic pores.

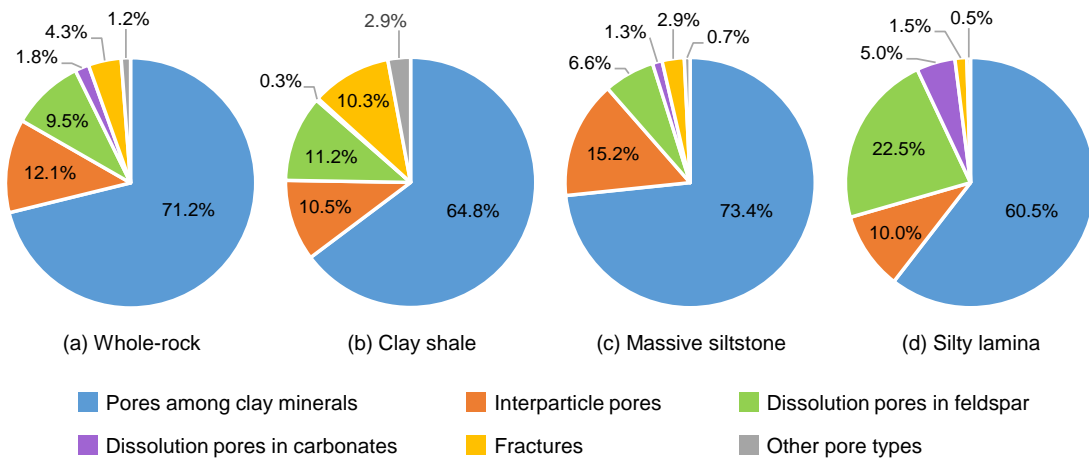


Fig. 6. Proportions of the surface macroporosities of the various pore types in the total surface macroporosities of the (a) whole-rock samples and their constituent lithologies, including (b) clay shale, (c) massive siltstone and (d) silty lamina. Surface macroporosity is determined by digitally analyzing scanning electron microscope images and calculating the ratio of total pore area to the total investigated area.

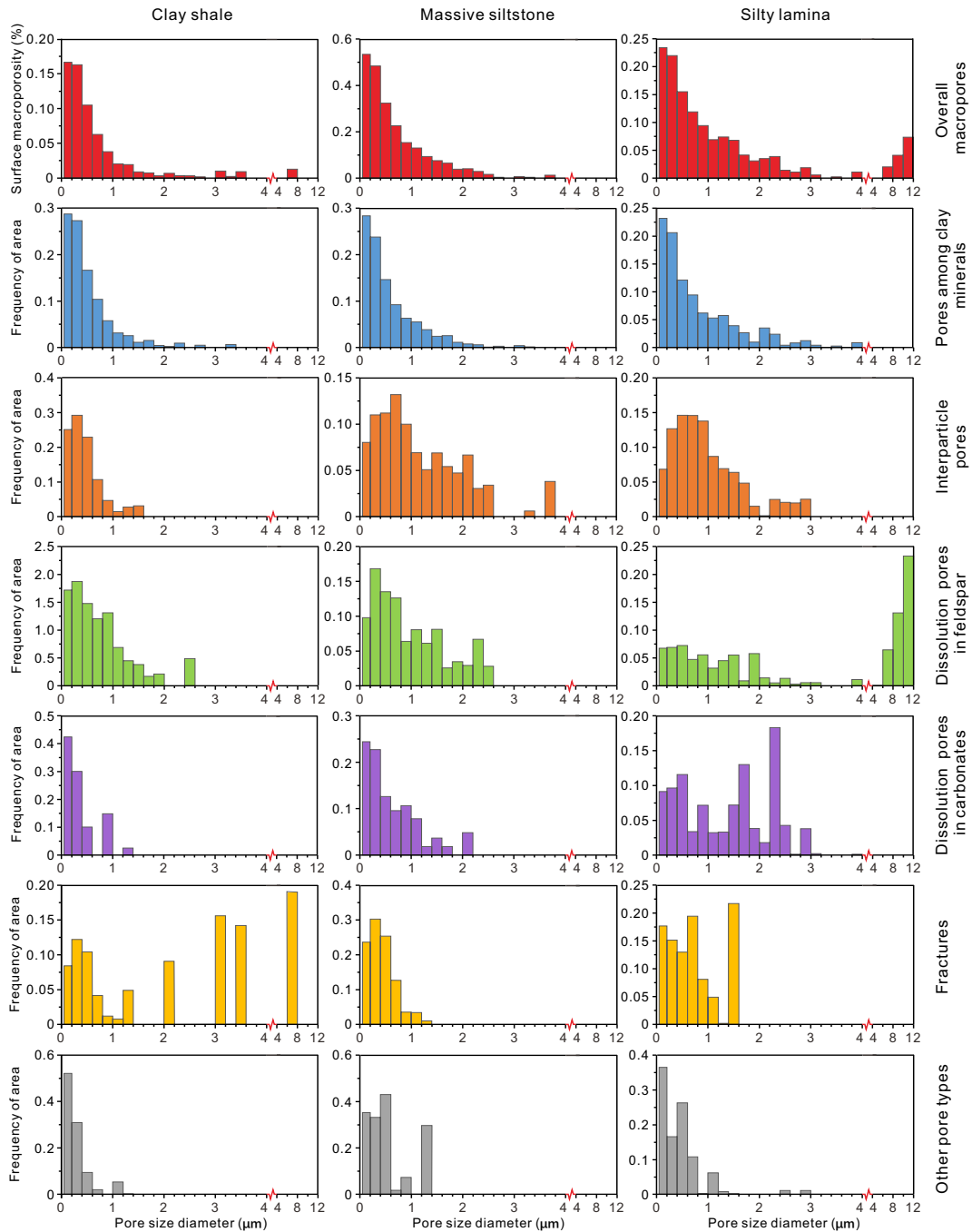


Fig. 7. Macropore size distribution and area frequency distribution of different pore types in distinct lithologies, determined through SEM digital analysis.

rock samples and quartz content (VIP = 1.17). Concurrently, negative correlations with both TOC content (VIP = 1.38) and pyrite content (VIP = 1.02) are also evident (Table 1). These correlations align with antecedent research (Han et al., 2018; Huang et al., 2023; Mei et al., 2023), underscoring the paramount influence of geological factors in governing macropore development within the Chang-7 shale. Specifically, the positive correlation between quartz and macropore volume has been attributed to the presence of a rigid quartz grain framework, facilitating the preservation of intergranular pores during compaction (Huang et al., 2023; Mei et al., 2023).

This observed pattern is in line with similar observations in other shale formations, such as the Longmaxi shale in the Sichuan Basin (Shi et al., 2015) and the Dawuba shale in the Qiannan Depression in China (Yuan et al., 2022). On the other hand, the inverse correlation identified between TOC and macropore volume has been ascribed to predominance of inorganic macropores in the Chang-7 shale (Han et al., 2018). And the noted negative correlation between pyrite content and macropore volume has been linked to the macropore blockage caused by idiomorphic pyrites in the Chang-7 shale (Huang et al., 2023; Wang et al., 2023a). Similar negative correlations

and interpretation have also been applied to the Shahejie shale of the Dongying Depression (Wang et al., 2021b; Khan et al., 2022).

However, it is imperative to emphasize the substantial interconnections among geological factors. As illustrated in Fig. S3(a), TOC exhibits a significant negative correlation with quartz ($R^2 = 0.60$). This negative relationship may be attributed to an elevated sedimentation rate induced by high detrital influx, leading to the potential dilution of TOC content in the sediments. When the high flux of detrital material in quartz-rich, a negative correlation between TOC and quartz content may occur. A similar scenario applies to the correlation between pyrite and TOC, where a clear positive correlation is observable (Fig. S3(b), $R^2 = 0.50$). This trend has been attributed to the prevalence of anoxic environment, which is conducive to pyrite formation, meanwhile promoting the development and preservation of organic matter (Liu et al., 2021a, 2021b; Zhang et al., 2022b). Apparently, the interplay among TOC, quartz, and pyrite contents is highly complicated. It is plausible that some of these factors play a dominant role in the macropore development, while others merely exhibit a superficial correlation with macropore volume. This correlation may arise from multicollinearity rather than a genuine impact on the formation and preservation of pores. Consequently, although correlation analysis is instrumental in revealing mathematical linearities among variables, it is constrained in accurately identifying the principal determinants of pore development because of the interference of multicollinearity.

5.2 Validating the outcomes of correlation analysis

The negative correlation between macropore volume and TOC posits a dominance of inorganic macropores within the Chang-7 shale. The microscopic analysis of macropores in whole rocks and their constituent lithologies consolidated this notion, revealing that inorganic macropores account for over 98.8% of the total macropores within the whole-rock Chang-7 samples (Fig. 6(a)). This stark contrast is notable when compared to the Longmaxi shale in the Sichuan Basin, where a positive correlation between macropore volume and TOC prevails, attributed to the abundance of organic macropores (Liu et al., 2021a). In fact, the development of organic pores in shale is mainly subject to the type, content and maturity of organic matters (Berthonneau et al., 2018; Yan et al., 2021; Borjigin et al., 2021; Qin et al., 2023). Compared to the Longmaxi shale (average TOC = 1.50%; average $R_o = 2.04\%$) (Shi et al., 2015; Wang et al., 2021a), the Chang-7 shale shares similar kerogen types (types I and II), but possesses higher TOC contents (8.99% in average) and lower R_o values (0.73% in average) (Table S1). This divergence suggests that the limited presence of organic macropores in the Chang-7 shale predominantly stems from its relatively low organic matter maturity. Additionally, another factor contributing to the negative correlation between TOC and macropore volume is the presence of pore-occluding solid bitumen (Figs. 8(a)-8(b)). Solid bitumen, a secondary product generated from kerogen or bitumen (Sanei, 2020), tends to accumulate and

occupy a greater portion of pores in high-TOC shale, further decreasing macroporosity. Therefore, TOC indeed emerges as a pivotal factor controlling macropore development in the Chang-7 shale.

The positive correlation between macropore volume and quartz has been traditionally attributed to role of the quartz-established rigid framework, which promotes the preservation of pores during compaction (Huang et al., 2023; Mei et al., 2023). However, it is worth noting that, despite feldspar being the second-most abundant mineral and also constituting a compaction-resistant mineral within the Chang-7 shale, its content (VIP = 0.32) exhibits a negligible correlation with macropore volume. This finding indicates the limited capacity of rigid minerals alone to exclusively dictate the variation in macropore volume, despite their facilitative impact on pore development. Considering the significant concurrent correlation of TOC with both the macropore volume and quartz, it suggests that the manifested correlation between quartz and macropore volume may be a consequence of these complex interdependencies, rather than a direct causation.

In addition, the negative correlation between macropore volume and pyrite was ascribed to the presence of idiomorphic pyrite, which governs macropore volume variation by infilling macropore space (Huang et al., 2023; Wang et al., 2023a). However, it is essential to appreciate that idiomorphic pyrites have a dual impact on porosity. While they do indeed occupy a fraction of primary macropores, they concurrently establish rigid frameworks that safeguard intercrystalline pores during episodes of intense compaction, potentially leading to an enhancement of macroporosity (Su et al., 2018). Specifically, within the Chang-7 shale, numerous lenticular aggregates composed of idiomorphic pyrites were observed (as shown in Fig. 8(c)), indicating the filling effect of idiomorphic pyrite in the original interlayer fractures or gaps. Apparently, the Chang-7 shale has undergone significant compaction during its burial, as evidenced by the quartz stylolite in Fig. 8(a), leading to the closure of the majority of original interlayer voids that lacked support from rigid components. Nevertheless, the original interlayer voids filled with pyrite may have preserved considerable intercrystalline macropores. On the other hand, The Chang-7 shale contains a high pyrite content, with an average of 11 wt% (Table 1). The majority of these pyrites are framboidal and idiomorphic pyrites (Liu et al., 2021a) (Fig. 8(c)), which, as mentioned above, promote the development of intercrystalline pores. However, the intercrystalline macropores associated with pyrite are extremely limited, comprising just less than 1.2% of the total macroporosity (Fig. 6(a)). It appears that the original intercrystalline macropores among pyrite crystals have been occluded by abundant organic matter (Fig. 8(d)). This observation implies that the organic matter has played a key role in impairing the original intercrystalline macropores of pyrite, thereby largely offsetting the promoting effect of pyrite on macropore development. Consequently, it is suggested that pyrite may not be the key factor governing macropore development, and its significant correlation with macropore volume may also result from the complex interplay of multiple geological factors.

To sum up, as mentioned above, the macropore develop-

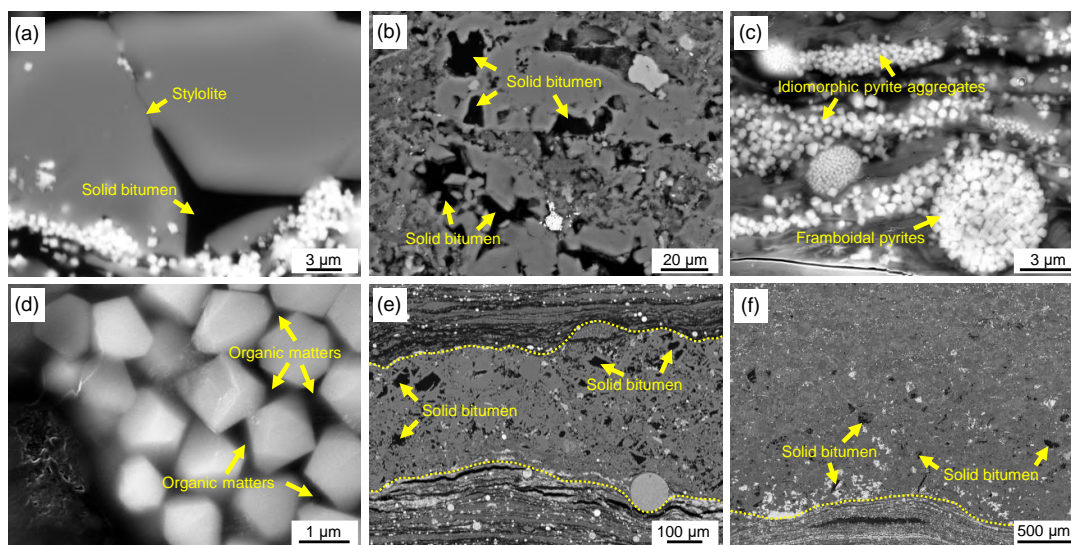


Fig. 8. Electron microscope photomicrographs of the Chang-7 shale. (a) Backscattered electron image showing quartz stylolite and pore-filling solid bitumen, (b) backscattered electron image showing that the feldspar dissolution pores are filled with solid bitumen, (c) secondary electron image showing the framboidal pyrites as well as the idiomorphic pyrite aggregates filling in the lenticular fractures between shale layers, (d) secondary electron image showing the organic matters filling in the space among the pyrite crystals, (e) backscattered electron image showing the solid bitumen filling the pores in silty lamina and (f) backscattered electron image showing that solid bitumen in siltstone is mainly distributed in the portion near the clay shale.

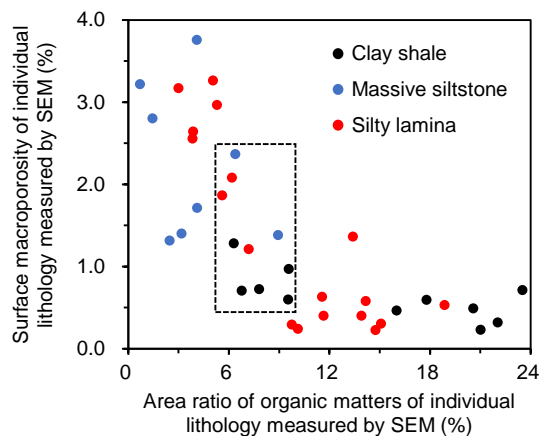


Fig. 9. Negative correlation between surface macroporosity and area ratio of organic matters for various lithologies of the Chang-7 shale. The data enclosed within rectangular frames indicates that the surface macroporosity of massive siltstone is moderately higher than that of clay shale, despite having a similar abundance of organic matter.

ment in the Chang-7 shale is predominantly governed by TOC content. While quartz and pyrite display correlations with macropore volume, they do not assume the role of primary controlling factors; instead, the observed correlation may be misleading and could be a consequence of their interconnection with TOC. To effectively identify the “sweet point” in the Chang-7 shale, it is advisable to prioritize the assessment of macropore development based on the abundance of organic matter. Disproportionate emphasis on quartz and pyrite contents in the chang-7 shale may not yield accurate

insights into the favorable zones.

5.3 Mechanisms and implications of macropore development in distinct lithologies

The negative correlation between the surface macroporosity and the area ratio of organic matters across various lithologies (Fig. 9) underscores the crucial role of organic matter abundance as a primary factor in controlling macropore development. Moreover, the figure also reveals that different lithologies possess different level of organic matter content, particularly when comparing clay shale and massive siltstone, which suggests that multi-correlations also exist among macroporosity, organic matter abundance and lithology. Intriguingly, the data enclosed in Fig. 9 reveal that the surface macroporosity of massive siltstone moderately surpasses that of clay shale, despite both exhibiting similar organic matter abundances. This discrepancy suggests that lithology may exert a potential influence on macroporosity variations, yet this effect appears insufficient to change the negative correlation trend depicted in Fig. 9. Consequently, the impact of lithology, albeit not negligible, seems comparably less significant than that of organic matter abundance.

Significant variations in macropore types and structures across different lithologies are noteworthy (Figs. 6 and 7), as they offer valuable insights into the distinct macropore development mechanisms inherent to each lithology. While the proportions of interparticle macropores relative to the total macropores across various lithologies are similar (10.0%-15.2%; Figs. 6(b)-6(d)), a significant contrast is observed in their absolute surface macroporosities. Massive siltstone boasts

an average surface macroporosity of 0.34% in interparticle pores, while silty lamina registers an average of 0.14%. These values are nearly quintuple and double the surface macroporosity measured in clay shale (average of 0.07%), respectively (Tables S3-S5). According to the macropore size distribution (Fig. 7), up to 46.6% and 37.5% of interparticle macropores within massive siltstone and silty lamina, respectively, possess pore sizes exceeding 1 μm . By contrast, clay shale exhibits a significantly lower percentage of 8.4%. Furthermore, macropores within clay minerals larger than 1 μm account for 17.1% and 28.5% in massive siltstone and silty lamina, respectively, as opposed to 11.5% in clay shale (Fig. 7). This phenomenon can be primarily attributed to the prevalence of clastic particles within massive siltstone and silty laminae, a characteristic that fosters the formation of interparticle macropores and, crucially, fortifies the preservation of various types of macropores against compaction forces. In light of these comprehensive observations, it seems that the presence of clastic particles in the Chang-7 shale lithology stands as a pivotal factor in effecting macropore size.

Distinct disparities also exist in the macropore types and structures between massive siltstone and silty laminae (Figs. 6 and 7). Silty laminae possess a higher proportion of carbonate and feldspar dissolution macropores (27.5%) (Fig. 6(d)), nearly tripling the 7.9% found in massive siltstone (Fig. 6(c)). This disparity primarily results from the close proximity of silty laminae to the source rock (i.e., clay shale). This proximity triggers intensified dissolution processes catalyzed by organic acids generated from kerogen during the thermal maturation of organic matter. Moreover, the more vigorous dissolution occurring in silty laminae contribute to the development of larger-sized dissolution macropores. As depicted in Fig. 7, approximately 68.8% and 59.1% of feldspar and carbonate dissolution macropores in silty laminae possess pore sizes exceeding 1 μm , markedly surpassing the corresponding proportions in massive siltstone, which are 40.8% and 20.0%, respectively. The sizes of feldspar dissolution macropores in silty laminae can even reach up to 12 μm , whereas they predominantly measure less than 3 μm in massive siltstone. Although silty lamina exhibits a lower average macroporosity when compared to massive siltstones in the Chang-7 shale, their significance in shale oil development should not be overlooked. Their proximity to the source rock suggests a greater potential for increased oil saturation and a higher abundance of large-sized dissolved macropores. Consequently, under certain conditions, silty laminae may indeed represent a more favorable shale oil reservoir as compared to massive siltstone.

5.4 Evaluation of the methods for shale pore investigation

Correlation analysis based on whole-rock testing technologies remains the prevailing method for investigating factors controlling shale pores. This method discloses mathematical correlations between pore-related parameters and geological factors through constructing regression models. However, the presence of multicollinearity introduces complexity, where

discerned correlated factors may not genuinely govern pore development. Consequently, rigorous validation is crucial for the outcomes of correlation analysis. The advent of SEM digital analysis technology, adept at characterizing the structure of various types of pores across distinct lithologies, provides a means to disentangle the intricate interplay among geological factors. This technology helps discovering authentic correlations between pores and geological factors, thereby revealing pore development mechanisms. By combining correlation analysis and SEM digital technology, a comprehensive study was conducted on the macropores of Chang-7 shale, elucidating multi-correlations encompassing macropore volume, TOC, minerals (including quartz and pyrite), and lithology. This study unveiled that the macroporosity is primarily determined by organic matter abundance, while the macropore types and structures are predominantly governed by lithology. These insights, providing a novel perspective for Chang-7 shale oil exploration and exploitation, conspicuously surpass the capabilities of traditional correlation analysis. Given its superior performance, it is advisable to enhance the utilization of SEM digital analysis technology in the study of pore development mechanisms in shale.

6. Conclusions

In this study, a systematically investigation of macropore structures in the Upper Triassic Chang-7 shale of the Ordos Basin was carried out using mercury injection capillary pressure and scanning electron microscopy digital analysis. Conventional correlation analysis indicated significant associations between macropore volumes and the contents of total organic carbon, pyrite, and quartz. However, a more detailed examination through scanning electron microscopy digital analysis revealed that total organic carbon content is the determinant in macropore development, while lithology governs macropore types and structures. The observed correlations of pores with pyrite and quartz can be largely ascribed to multicollinearity rather than a causal relationship.

The investigation clearly highlighted the constraints of traditional correlation analysis approaches, emphasizing the capability of scanning electron microscopy to disentangle the influence of multicollinearity. Beyond that, scanning electron microscopy also provided detailed views into the variety of macropore types and their size distributions across distinct lithologies, offering a deeper comprehension of the lithological impacts on pore structures. Therefore, it is recommended to integrate scanning electron microscopy digital analysis into standard shale pore studies. This technique holds the potential to significantly enhance the efficiency of exploration and recovery in shale oil and gas resources.

Acknowledgements

The authors are grateful for the financial support by National Natural Science Foundation of China (Nos. 42090021 and 42373050).

Supplementary file

<https://doi.org/10.46690/ager.2024.03.04>

Conflict of interest

The authors declare no competing interest.

Open Access This article is distributed under the terms and conditions of the Creative Commons Attribution (CC BY-NC-ND) license, which permits unrestricted use, distribution, and reproduction in any medium, provided the original work is properly cited.

References

- Berthonneau, J., Obliger, A., Valdenaire, P. L., et al. Mesoscale structure, mechanics, and transport properties of source rocks' organic pore networks. *Proceedings of the National Academy of Sciences of the United States of America*, 2018, 115(49): 12365-12370.
- Borjigin, T., Lu, L., Yu, L., et al. Formation, preservation and connectivity control of organic pores in shale. *Petroleum Exploration and Development*, 2021, 48(4): 798-812.
- Cao, Z., Liu, G., Zhan, H., et al. Pore structure characterization of Chang-7 tight sandstone using MICP combined with N2GA techniques and its geological control factors. *Scientific Reports*, 2016, 6(1): 36919.
- Chen, G., Gang, W., Liu, Y., et al. Organic matter enrichment of the Late Triassic Yanchang Formation (Ordos Basin, China) under dysoxic to oxic conditions: Insights from pyrite framboid size distributions. *Journal of Asian Earth Sciences*, 2019, 170: 106-117.
- Cui, J., Zhu, R., Li, S., et al. Development patterns of source rocks in the depression lake basin and its influence on oil accumulation: Case study of the Chang 7 member of the Triassic Yanchang Formation, Ordos Basin, China. *Journal of Natural Gas Geoscience*, 2019, 4(4): 191-204.
- Favilla, S., Durante, C., Vigni, M. L., et al. Assessing feature relevance in NPLS models by VIP. *Chemometrics and Intelligent Laboratory Systems*, 2013, 129: 76-86.
- Fu, J., Li, S., Guo, Q., et al. Enrichment condition and favorable area optimization of continental shale oil in Ordos Basin. *Acta Petrolei Sinica*, 2022, 43(12): 1702-1716. (in Chinese)
- Fu, J., Li, S., Hou, Y., et al. Breakthrough of risk exploration of Class II shale oil in Chang 7 member of Yanchang Formation in the Ordos Basin and its significance. *China Petroleum Exploration*, 2020, 25(1): 78-92. (in Chinese)
- Gao, C., Chen, Y., Yin, J., et al. Experimental study on reservoir characteristics and oil-bearing properties of Chang 7 lacustrine oil shale in Yan'an area, China. *Open Geosciences*, 2022, 14(1): 234-251.
- Goldstein, J. I., Newbury, D. E., Michael, J. R., et al. *Scanning Electron Microscopy and X-ray Microanalysis*. New York, USA, Springer, 2018.
- Guo, H., Jia, W., Peng, P., et al. The composition and its impact on the methane sorption of lacustrine shales from the Upper Triassic Yanchang Formation, Ordos Basin, China. *Marine and Petroleum Geology*, 2014, 57: 509-520.
- Han, H., Liu, P., Ding, Z., et al. The influence of extractable organic matter on pore development in the Late Triassic Chang 7 lacustrine shales, Yanchang Formation, Ordos Basin, China. *Acta Geologica Sinica*, 2018, 92(4): 1508-1522.
- Hu, T., Pang, X., Jiang, F. Advances in whole petroleum system theory and new directions for petroleum geology development. *Advances in Geo-Energy Research*, 2024, 11(1): 1-5.
- Huang, W., Ma, X., Zhou, X., et al. Characteristics and controlling factors of pore structure of shale in the 7th member of Yanchang Formation in Huachi area, Ordos Basin, China. *Journal of Natural Gas Geoscience*, 2023, 8(5): 319-336.
- Khan, D., Qiu, L., Liang, C., et al. Formation and distribution of different pore types in the lacustrine calcareous shale: Insights from XRD, FE-SEM, and low-pressure nitrogen adsorption analyses. *ACS Omega*, 2022, 7(12): 10820-10839.
- Li, J., Lu, S., Cai, J., et al. Adsorbed and free oil in lacustrine nanoporous shale: A theoretical model and a case study. *Energy & Fuels*, 2018, 32(12): 12247-12258.
- Li, X., Cai, J., Liu, H., et al. Characterization of shale pore structure by successive pretreatments and its significance. *Fuel*, 2020, 269: 117412.
- Lin, S., Hou, L., Luo, X., et al. A millimeter-scale insight into formation mechanism of lacustrine black shale in tephra deposition background. *Scientific Reports*, 2022, 12(1): 11511.
- Liu, J., Li, S., Li, Z., et al. Characteristics and geological significance of pyrite in Chang 7₃ sub-member in the Ordos Basin. *Natural Gas Geoscience*, 2021a, 32(12): 1830-1838. (in Chinese)
- Liu, K., Ostadhassan, M. Multi-scale fractal analysis of pores in shale rocks. *Journal of Applied Geophysics*, 2017, 140: 1-10.
- Liu, K., Ostadhassan, M., Zhou, J., et al. Nanoscale pore structure characterization of the Bakken shale in the USA. *Fuel*, 2017, 209: 567-578.
- Liu, Q., Li, P., Jin, Z., et al. Preservation of organic matter in shale linked to bacterial sulfate reduction (BSR) and volcanic activity under marine and lacustrine depositional environments. *Marine and Petroleum Geology*, 2021b, 127: 104950.
- Liu, R., Zhou, W., Xu, H., et al. Impact of minerals and sealing systems on the pore characteristics of the Qiongzhusi formation shale in the southern Sichuan Basin. *ACS Omega*, 2022, 7(18): 15821-15840.
- Liu, Y., Shen, B., Yang, Z., et al. Pore structure characterization and the controlling factors of the Bakken Formation. *Energies*, 2018, 11(11): 2879.
- Longman, M., Dahlberg, K., Yared, K. Lithologies and petrophysical characteristics of the Upper Cretaceous Baxter Shale gas reservoir, Canyon Creek Field, Sweetwater County, Wyoming. Paper SPE 180218 Presented at SPE Low Perm Symposium, Denver, Colorado, 5-6 May, 2016.
- Lu, H., Xia, D., Li, Q., et al. Quantitative characterization and differences of the pore structure in lacustrine siliceous shale and argillaceous shale: A case study of the Upper Triassic Yanchang Formation shales in the southern Ordos Basin, China. *Energy & Fuels*, 2021, 35(19): 15525-

- 15544.
- Mei, Q., Guo, R., Zhou, X., et al. Pore structure characteristics and impact factors of laminated shale oil reservoir in Chang 7₃ sub-member of Ordos Basin, China. *Journal of Natural Gas Geoscience*, 2023, 8(4): 227-243.
- Qin, X., Zhao, L., Zhu, J., et al. Modeling the elastic characteristics of overpressure due to thermal maturation in organic shales. *Advances in Geo-Energy Research*, 2023, 10(3): 174-188.
- Qin, Y., Yao, S., Xiao, H., et al. Pore structure and connectivity of tight sandstone reservoirs in petroleum basins: A review and application of new methodologies to the Late Triassic Ordos Basin, China. *Marine and Petroleum Geology*, 2021, 129: 105084.
- Sanei, H. Genesis of solid bitumen. *Scientific Reports*, 2020, 10: 15595.
- Shi, M., Yu, B., Xue, Z., et al. Pore characteristics of organic-rich shales with high thermal maturity: A case study of the Longmaxi gas shale reservoirs from well Yuye-1 in southeastern Chongqing, China. *Journal of Natural Gas Science and Engineering*, 2015, 26: 948-959.
- Sing, K. S., Everett, D. H., Haul, R. A., et al. Reporting physisorption data for gas/solid systems with special reference to the determination of surface area and porosity (Recommendations 1984). *Pure and Applied Chemistry*, 1985, 57(4): 603-619.
- Stocchero, M., Locci, E., d'Aloja, E., et al. PLS2 in metabolomics. *Metabolites*, 2019, 9(3): 51.
- Su, S., Jiang, Z., Xuanlong, S., et al. The effects of shale pore structure and mineral components on shale oil accumulation in the Zhanhua Sag, Jiyang Depression, Bohai Bay Basin, China. *Journal of Petroleum Science and Engineering*, 2018, 165: 365-374.
- Tang, L., Song, Y., Jiang, Z., et al. Influencing factors and mathematical prediction of shale adsorbed gas content in the Upper Triassic Yanchang Formation in the Ordos Basin, China. *Minerals*, 2019, 9(5): 265.
- Wang, G., Jin, Z., Liu, G., et al. Pore system of the multiple lithofacies reservoirs in unconventional lacustrine shale oil formation. *International Journal of Coal Geology*, 2023a, 273: 104270.
- Wang, R., Wang, G., Zhao, G., et al. Geological characteristics and resources potential of shale oil in Chang 7 Member of Upper Triassic Yanchang Formation in Fuxian area, southern Ordos Basin, western China. *Unconventional Resources*, 2023b, 3: 237-247.
- Wang, X., Li, J., Jiang, W., et al. Characteristics, current exploration practices, and prospects of continental shale oil in China. *Advances in Geo-Energy Research*, 2022, 6(6): 454-459.
- Wang, X., Zhu, Y., Chen, S., et al. Molecular structure evaluation and image-guided atomistic representation of marine kerogen from Longmaxi Shale. *Energy & Fuels*, 2021a, 35(9): 7981-7992.
- Wang, Z., Zhang, L., Gao, Y., et al. Pore properties of the lacustrine shale in the upper part of the sha-4 Member of the Paleogene Shahejie Formation in the Dongying Depression in East China. *Geofluids*, 2021b, 2021: 6616843.
- Wold, S., Sjostrom, M., Eriksson, L. PLS-regression: a basic tool of chemometrics. *Chemometrics and Intelligent Laboratory Systems*, 2001, 58(2): 109-130.
- Wu, T., Pan, Z., Liu, B., et al. Laboratory characterization of shale oil storage behavior: A comprehensive review. *Energy & Fuels*, 2021, 35(9): 7305-7318.
- Yan, J., Zhang, S., Wang, J., et al. Applying fractal theory to characterize the pore structure of lacustrine shale from the Zhanhua Depression in Bohai Bay Basin, Eastern China. *Energy & Fuels*, 2018, 32(7): 7539-7556.
- Yang, H., Dou, W., Liu, X., et al. Analysis on sedimentary facies of member 7 in Yanchang Formation of Triassic in Ordos Basin. *Acta Sedimentologica Sinica*, 2010, 28(2): 254-263. (in Chinese)
- Yu, Y., Luo, X., Cheng, M., et al. Study on the distribution of extractable organic matter in pores of lacustrine shale: An example of Zhangjiatan Shale from the Upper Triassic Yanchang Formation, Ordos Basin, China. *Interpretation*, 2016, 5(2): SF109-SF126.
- Yu, Y., Luo, X., Wang, Z., et al. A new correction method for mercury injection capillary pressure (MICP) to characterize the pore structure of shale. *Journal of Natural Gas Science and Engineering*, 2019, 68: 102896.
- Yuan, K., Huang, W., Chen, X., et al. The Whole-aperture pore structure characteristics and their controlling factors of the Dawuba Formation shale in Western Guizhou. *Processes*, 2022, 10(4): 622.
- Zhang, Q., Qiu, Z., Zhang, L., et al. Characteristics and controlling factors of transitional shale gas reservoirs: An example from Permian Shanxi Formation, Daning-Jixian block, Ordos Basin, China. *Journal of Natural Gas Geoscience*, 2022a, 7(3): 147-157.
- Zhang, W., Jin, Z., Liu, Q., et al. The C-S-Fe system evolution reveals organic matter preservation in lacustrine shales of Yanchang Formation, Ordos Basin, China. *Marine and Petroleum Geology*, 2022b, 142: 105734.
- Zhao, W., Hu, S., Hou, L. Connotation and strategic role of in-situ conversion processing of shale oil underground in the onshore China. *Petroleum Exploration and Development*, 2018, 45(4): 563-572.
- Zhao, W., Zhu, R., Hu, S., et al. Accumulation contribution differences between lacustrine organic-rich shales and mudstones and their significance in shale oil evaluation. *Petroleum Exploration and Development*, 2020, 47(6): 1079-1089.